

Multiscale polar theory of microtubule and motor-protein assemblies

Tong Gao¹, Robert Blackwell², Matthew A. Glaser², M. D. Betterton², Michael J. Shelley¹

¹*Courant Institute of Mathematical Sciences, New York University, New York, NY 10012*

²*Department of Physics and Liquid Crystal Materials Research Center
and Biofrontiers Institute University of Colorado, Boulder, CO 80309*

Microtubules and motor proteins are building blocks of self-organized subcellular biological structures such as the mitotic spindle and the centrosomal microtubule array. These same ingredients can form new “bioactive” liquid-crystalline fluids that are intrinsically out of equilibrium and which display complex flows and defect dynamics. It is not yet well understood how microscopic activity, which involves polarity-dependent interactions between motor proteins and microtubules, yields such larger scale dynamical structures. In our multiscale theory, Brownian dynamics simulations of polar microtubule ensembles driven by crosslinking motors allow us to study microscopic organization and stresses. Polarity sorting and crosslink relaxation emerge as two polar-specific sources of active destabilizing stress. On larger length scales, our continuum Doi-Onsager theory captures the hydrodynamic flows generated by polarity-dependent active stresses. The results connect local polar structure to flow structures and defect dynamics.

PACS numbers: 87.10.-e, 47.57.E-

Nonequilibrium materials composed of self-driven constituents – active matter – presents novel physics to understand and may one day provide new technologies such as autonomously moving and self-healing materials [1–5]. One central example is mixtures of cytoskeletal filaments and molecular motors, which are important for their ability to form self-assembled cellular structures such as the mitotic spindle and cell cortex. Reduced *in vitro* systems show that biofilament and motor-protein mixtures can form self-organized patterns, such as vortices and asters, reminiscent of cellular structures [6–8]. Recently, Sanchez *et al.* [9] synthesized mixtures of microtubules (MTs), multimeric kinesin-1 motor complexes, ATP, and a depletant. In bulk, extended MT bundles spontaneously form which continuously stretch, bend and fracture, leading to large-scale flows. When condensed onto an oil-water interface, the MTs form a nematic-like ordered active surface characterized by turbulent-like motions and motile disclination defects.

Understanding reduced filament-motor systems is an important step towards comprehending more complex active systems. Therefore theoretical studies have investigated aspects of MT and motor-protein assemblies at different scales [10–14]. Inspired by the experiments of Sanchez *et al.* [9], Giomi *et al.* [15, 16] and Thampi *et al.* [17–19] have studied liquid crystal hydrodynamic models driven by an apolar active stress [20]. While apolar models reproduce qualitative features of these experiments, MTs have polarity and crosslinking motors move directionally; hence, aligned MTs must have different interactions than anti-aligned MTs, and activity-driven material stresses and fluxes should reflect the polarity of these interactions. We investigate this through multiscale modeling, first discovering two separate microscopic sources of active and extensile stresses, one induced by motor driven *polarity-sorting* of anti-aligned

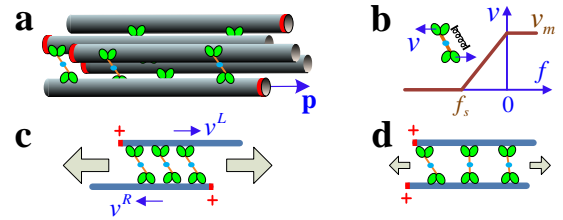


FIG. 1: (a) Schematic of a cluster of polar-aligned and anti-aligned MTs, with their plus ends marked by red rings. Crosslinking motors walk on neighboring MTs at speed v , and (b) exert spring-like forces, with a linear force-velocity relation. (c) An anti-aligned MT pair being polarity-sorted by active crosslinks. The left- (right-) pointing MT moves right (left) with velocity v^L (v^R). (d) A polar-aligned MT pair upon which crosslink forces are relaxing due to the force-velocity relation. In both, the grey arrows characterize the magnitude of an induced extensile stress.

MTs, and another from relaxation of crosslink tethers between polar-aligned MTs. We formulate a Doi-Onsager model [21–24] with fluxes and stresses reflecting these effects, and use this to study the Sanchez *et al.* interfacial experiments. Simulations show persistent folding flows and defect birth and annihilation, arising from active stresses occupying geometrically distinct regions. Having properly accounted for drag of the bounding fluids, we find a well-defined characteristic length-scale from linear theory which agrees well with feature sizes in our simulations.

We outline the basic model in Fig. 1. Every MT has a plus-end oriented director \mathbf{p} , the same length l and diameter b (Fig. 1a). Nearby MTs are coupled by active plus-end directed crosslinks consisting of two motors connected by a spring-like tether. Motor velocities are controlled by a piecewise linear force-velocity relation (Fig. 1b). For anti-aligned MTs (Fig. 1c) the two motors

move in opposite directions, stretching the tether to slide the MTs towards their minus-ends, which is termed *polarity sorting* [10]. Conversely, for polar-aligned MTs the two motors move in the same direction, with little or no net sliding, and the retarding force on the leading motor causes stretched tethers to relax (Fig. 1d).

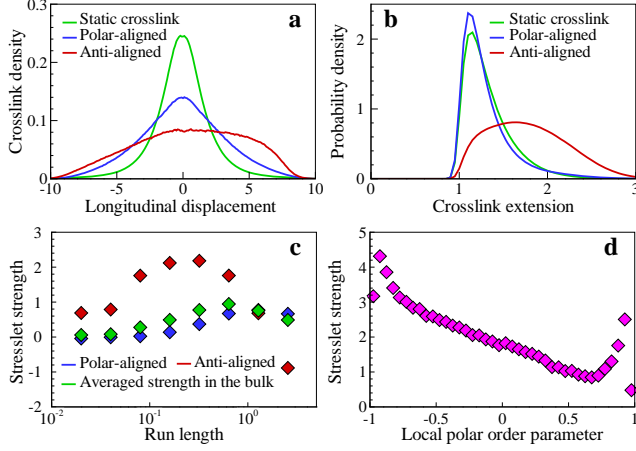


FIG. 2: Results of the BD-MC particle simulations. (a) Histogram of crosslink occupancy as a function of the particle pair longitudinal displacement s_{ij} . (b) Histogram of crosslink extension r_c . (c) Variation of extensile pair stresslet S (unit of force \times length) with motor run length ℓ . (d) Typical variation of extensile pair stresslet with local polarity m_i .

Microscopic model. We first perform 2D Brownian dynamics-Monte Carlo (BD-MC) simulations of MTs driven by explicit motors with binding/unbinding kinetics [26]. The main purpose is to quantify local MT pair interactions, with long-ranged hydrodynamics neglected due to its high computational cost. We represent MTs as perfectly rigid rods, and assume a reservoir of ideal motors at fixed chemical potential. The motors bind to (unbind from) two filaments simultaneously, and unbind immediately upon reaching the plus end of either MT. At equilibrium, the average number of motors crosslinking MTs i and j is $\langle N_{ij} \rangle \sim \rho^2 \int ds_i \int ds_j \exp \left[-\frac{u_c(s_i, s_j)}{k_B T} \right]$, where ρ is the linear binding-site density on a single MT, u_c is the quadratic potential for crosslinks extension, and $s_{i,j}$ parametrizes the MT arclength [26]. The number of motors that bind/unbind is sampled from a Poisson distribution with the correct average number of events at each time interval so that the equilibrium distribution is recovered for static crosslinks. Bound motors are inserted by first selecting pairs of MTs then sampling from the appropriate bivariate normal distribution to choose motor endpoints. The motor on each crosslink endpoint moves with a linear force-velocity relation [25]: $v = v_m \max(0, \min(1, 1 + f/f_s))$, where f is the magnitude of the crosslinking force, v_m is the maximum translocation velocity, and f_s is the stall force. After the MC cycle, we compute all the forces and torques from mo-

tors, short-range repulsion, anisotropic local fluid drag by the solvent, and random thermal forces, to evolve MT positions and orientations forward in time [26, 27]. The BD-MC simulations are nondimensionalized using the length b , energy $k_B T$, and time $\tau = D/b^2$, where D is the diffusion coefficient of a sphere of diameter b . Our model is similar to that of Head *et al.* [14], but new in our work are algorithmic improvements for handling crosslinks and neglect of filament elasticity that allow us to simulate larger systems and measure the stress tensor.

Extensile stress and its origins. Figure 2 illustrates the long-time behavior of MTs in the BD-MC simulations (video S1). For two MTs i and j with orientations \mathbf{p}_i and \mathbf{p}_j and center-of-mass displacement \mathbf{r}_{ij} , the longitudinal displacement is $s_{ij} = \frac{1}{2} \mathbf{r}_{ij} \cdot [\mathbf{p}_i + \text{sgn}(\mathbf{p}_i \cdot \mathbf{p}_j) \mathbf{p}_j]$. For anti-aligned MT pairs ($\mathbf{p}_i \cdot \mathbf{p}_j < 0$), s_{ij} is negative when the MT pair is contracting, and becomes positive when the MT pair is extending (see Fig. 1). When crosslinks are static or on polar-aligned MTs ($\mathbf{p}_i \cdot \mathbf{p}_j \geq 0$), the distribution of crosslinks is symmetric about $s_{ij} = 0$ (Fig. 2a). However for motors on anti-aligned MTs, the distribution skews toward positive values of s_{ij} , yielding a bias in force generated by the motors towards pair extension.

Motor motion alters the distribution of crosslink extension r_c (Fig. 2b). The minimum $r_c \approx 1$ due to MT steric interactions. For anti-aligned (polar-aligned) pairs, crosslink relaxation shifts the distribution toward larger (smaller) extension. The bulk material stress tensor is $\Sigma_b = \frac{N k_B T}{V} \mathbf{I} + \frac{1}{V} \left\langle \sum_i^N \mathbf{W}_i \right\rangle$ for N interacting MTs in a volume V , with $\mathbf{W}_i = \frac{1}{2} \sum_{j \neq i}^N \mathbf{r}_{ij} \mathbf{F}_{ij}$ the single-MT virial tensor [26, 28]. Over a wide range of motor parameters, the time-averaged bulk stress tensor Σ_b is anisotropic, with larger components in the average MT alignment direction. Denoting the alignment direction by $\hat{\mathbf{y}}$, the stress difference $\Sigma_b^{yy} - \Sigma_b^{xx}$ is positive, which corresponds to an extensile stress. The stress difference can be expressed as a sum of pair interactions, with each ij pair contributing a stresslet S_{ij} , prior to division by the bulk volume. The average pair stresslet S (green symbols in Fig. 2c) increases with the motor run length ℓ up to a maximum when the typical motor run length is the MT length. Here $\ell = v_m/k_0 l$, the typical distance a motor travels during one binding event, with k_0 a base binding rate of motors. Increasing ℓ further leads to decreasing S because the motors rapidly move to the ends of the MTs and unbind.

The extensile stress from anti-aligned pair interactions arises from asymmetries during polarity sorting. If an MT pair begins sliding when the two minus-ends touch and slide with a force proportional to pair overlap until the two plus-ends meet, then the total extensile stresslet would be zero. Two effects break this symmetry. First, MTs are unlikely to begin interacting exactly when their minus ends meet, decreasing the range of negative s_{ij} over which sliding occurs. Second, more motors are

bound on average during extension (Fig. 2a). Fig. 2d shows a typical polar curve of S as a function of m_i , where the local polar orientational order parameter m_i varies between 1 (all neighboring MTs are polar-aligned) and -1 (all neighbors are anti-aligned). A maximum for m_i occurs near -1 because polarity sorting is the dominant source of pair-wise extensile stress. As m_i increases, S drops with approximate linearity, at least away from the two isolated peaks that close examination shows are related to strong steric interactions of nearly parallel MTs: nearly, but not exactly, parallel MTs experience aligning torques due to crosslink-mediated attraction; the resulting steric collisions tend to promote pair extension that increases the extensile stress.

To understand the surprising and counterintuitive result that S remains positive even for polar-aligned pairs, we consider crosslink relaxation on perfectly parallel filaments. When crosslinks are active, the force of a longitudinally stretched crosslink opposes the leading motor, slowing it, and pulls forward on the trailing motor. This causes a slight but significant shift in the distribution of crosslink extension toward smaller values relative to the static-crosslink case (Fig. 2b). With crosslinking motors, the crosslink-induced contractile stress along the MT alignment direction is decreased, while there is no change in the transverse stress induced by crosslinks. This leads to a net anisotropic extensile stress in the alignment direction. When varying system parameters, we find that the extensile stresslet of polar-aligned MT pairs is typically 2–5 times smaller than that of anti-aligned pairs.

From microscopic to macroscopic models. To coarse-grain the BD-MC simulation results, we introduce a distribution function $\Psi(\mathbf{x}, \mathbf{p}, t)$ of MT center-of-mass positions \mathbf{x} and polar orientation vectors \mathbf{p} ($|\mathbf{p}| = 1$), and describe the particle dynamics in terms of the concentration $\Phi = \int_p \Psi$, the polarity vector $\mathbf{q} = \int_p \Psi \mathbf{p} / \Phi$, the second-moment tensor $\mathbf{D} = \int_p \Psi \mathbf{p} \mathbf{p}$, and the tensor order parameter tensor $\mathbf{Q} = \mathbf{D} / \Phi - \mathbf{I} / d$, with $d = 2$ or 3 the spatial dimension.

We first consider a nematically ordered local cluster of MTs undergoing polarity sorting (Fig. 1), with n MTs pointing rightwards (labelled R) and m MTs pointing leftwards (labelled L). When the motor ends move at a characteristic speed v_w , for an anti-polar MT pair, a minus-end-directed sliding is induced. Using Stokesian slender body theory [29] we find the velocities of the left- and rightward pointing MTs [26]: $v^L = \frac{2n}{n+m} v_w$, $v^R = -\frac{2m}{n+m} v_w$. This expression shows that the speed of each population depends on how many opposing MTs there are to pull against, with their drag as the anchor, and their relative velocity fixed at $v^L - v^R = 2v_w$. When considering a more general orientation distribution, a similar calculation [26] yields $\dot{\mathbf{x}} = \mathbf{q} - \mathbf{p}$ as the translational flux for MTs.

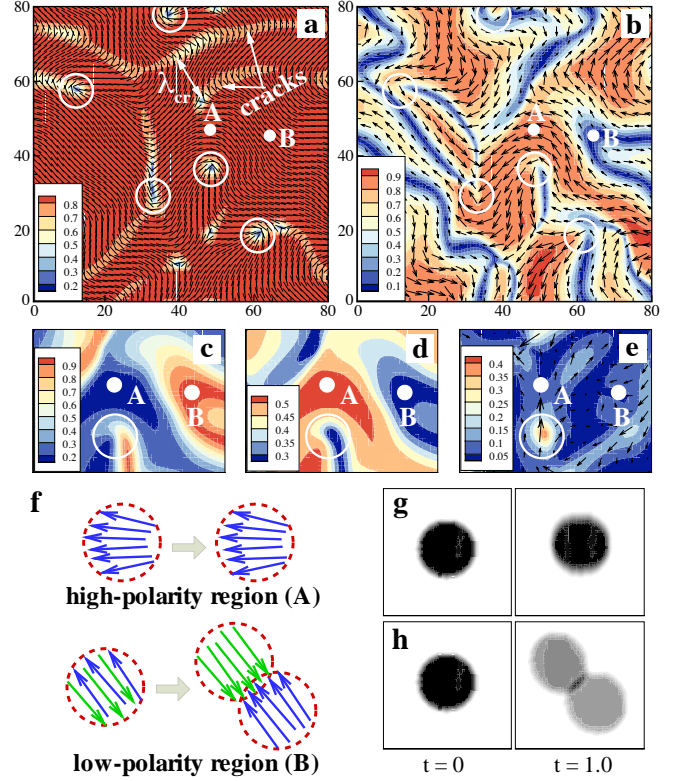


FIG. 3: Snapshots of streaming MT nematics on a liquid-liquid interface. (a) The nematic director field \mathbf{n} , superimposed on the colormap of the scalar order parameter (twice the positive eigenvalue of \mathbf{Q}); λ_{cr} is a calculated characteristic length between the cracks. (b) The polarity vector field \mathbf{q} superimposed upon its magnitude. (c,d) Polarity-dependent active stress magnitudes, showing principal eigenvalues of the active stresses (Σ_{aa} in c, and Σ_{pa} in d). (e) The vector field of the active force $\mathbf{f}^a = \nabla \cdot \Sigma^a$ superimposed upon its magnitude. In (a-e), circular areas labeled A and B mark regions of high and low polarity, respectively. Positions of $+1/2$ -order defects are marked by circles. (f-h) Predicted results of a photobleaching experiment of fluorescent MTs for a bleached spot in a region of high polar order (g, area A), and in a region of low polar order (h, area B). Arrows represent MTs with arrowheads denoting plus ends. A dimensionless time is used with scale $b/\nu v_w$, where ν is the effective volume fraction.

Slender-body theory also yields the forces each rod exerts on the fluid, and hence the induced “extra stress” tensor by polarity sorting can be expressed in dimensional form as $\sigma_{aa} = \frac{\eta v_w l^2}{V_c} \frac{\alpha_{aa}}{2} \frac{2mn}{m+n} \mathbf{p} \mathbf{p}$ [26, 30]. Here V_c is the cluster volume, and $\alpha_{aa} = s/l$ with s the signed distance between the centers-of-mass of the \mathbf{p} and $-\mathbf{p}$ oriented subclusters. For the extra stress due to crosslink relaxation, we lack a simple first-principles model of polar-aligned MTs, though the number of polar-pair interactions scales as $m^2 + n^2$. Given that the anti- and polar-aligned stresses are of the same order (Fig. 2d) we assume the form $\sigma_{pa} = \frac{\eta v_w l^2}{V_c} \frac{\alpha_{pa}}{2} \frac{m^2 + n^2}{m+n} \mathbf{p} \mathbf{p}$. Thus we are able to extract the (negative) values of

$\alpha_{aa,pa}$ by comparing the anti- and polar-aligned pair stresslet strengthes ($S_{aa,pa} = \frac{\eta v_w l^2 \alpha_{aa,pa}}{m+n}$, and v_w is taken as v_m) with the BD-MC simulations. Again, we construct the dimensionless 3D extra stress from \mathbf{D} and $\Phi \mathbf{q} \mathbf{q}$ (i.e., the simplest symmetric tensors quadratic in \mathbf{p}) as $\Sigma^a = \Sigma_{aa} + \Sigma_{pa} = \frac{\alpha_{aa}}{2}(\mathbf{D} - \Phi \mathbf{q} \mathbf{q}) + \frac{\alpha_{pa}}{2}(\mathbf{D} + \Phi \mathbf{q} \mathbf{q})$. The first (second) term captures active stress production via polarity sorting (crosslink relaxation) and exactly reproduces the form of σ_{aa} (σ_{pa}).

We further account for particle rotation as well as steric interactions, and couple MT motion with a background flow to study the effect of long-range hydrodynamic interactions absent in the BD-MC simulations through a continuum polar fluid model [21, 22, 24, 26, 31, 32]. Since in the Sanchez *et al.* experiments [9] the active material is confined to an interface between oil and water, we assume a thin layer of suspension immersed in the bulk viscous liquid, and close the system by solving the hydrodynamic coupling between the surface flow \mathbf{U} and external fluid motions through a velocity-stress relation in Fourier space: $\hat{\mathbf{U}} = \frac{i}{2}(\mathbf{I} - \hat{\mathbf{k}}\hat{\mathbf{k}})(\hat{\Sigma}^e \hat{\mathbf{k}})$, where $\hat{\mathbf{k}} = \mathbf{k}/k$ is the normalized 2D wave-vector [26].

Defects and polarity. Assuming 2D periodic boundary conditions and using a Fourier pseudo-spectral numerical method [22, 26], we simulated our model over long times. In regions of flow instability, we find persistently unsteady turbulent-like flows that are correlated with continual genesis, propagation, and annihilation of $\pm 1/2$ order defect pairs (see videos S2–S5). In Fig. 3a, the defects exist in regions of small nematic order (dark blue), and are born as opposing pairs in elongated “incipient crack” regions, qualitatively similar to the structures found in both experiments and apolar models [15–19]. Moreover, as shown in panel (b), the polarity field develops considerable spatial variation with regions of high and low polar order $|\mathbf{q}|$ (video S5). The two active stresses vary in strength depending on the local polarity — the polar-aligned (anti-aligned) stress is large in regions of high (low) polar order (panels (c) & (d)) — and hence are largest respectively in their complementary regions. The circles in Fig. 3b encircle $+1/2$ -order defects, showing the sharp variation of the polarity field around them, with the gradients of active stresses there yielding large active force shown in panel (e).

We further simulated the results of a photobleaching experiment in which a circular region is exposed to high-intensity laser light to inactivate the fluorescent molecules on the corresponding MTs [33] (Figs. 3f–h). In a small high-polarity region (marked A in Fig. 3), little or no polarity sorting occurs, and the photobleached spot remains approximately circular (Fig. 3f top, g) over longer times. In a low-polarity region of high nematic order (marked B in Fig. 3), strong polarity sorting of anti-aligned MTs causes a photobleached spot to separate into two lobes, showing decreased bleaching. This

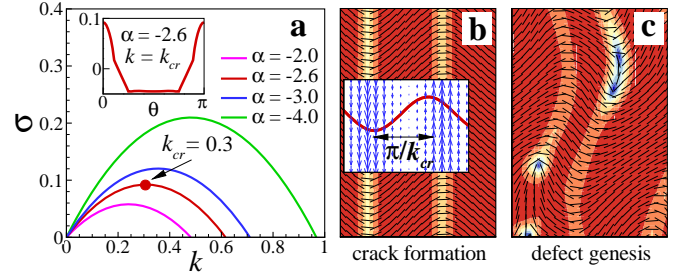


FIG. 4: Linear stability analysis (a) and nonlinear simulation (b,c) for strongly anti-aligned MTs. (a) The real part of the growth rate as a function of wave-number k for several values of α ($\alpha = \alpha_{aa} + \alpha_{pa}$). Here k_{cr} corresponds to a maximum growth rate. Inset: real part of the growth rate as a function of wave-angle θ when fixing $k = k_{cr}$. (b) Crack formation. Inset: the fluid velocity vector field (blue) and the eigenmode (red line) associated with k_{cr} . (c) Genesis of defects at late times.

type of experiment probes the local polarity field, and hence the origins of active stress.

Hydrodynamic instabilities and characteristic length. A key observation in our simulations as well as other active fluid systems [18, 34–36] is that defect pairs are generated along elongated cracks that themselves develop from regions of high polar order. Here we performed a linear stability analysis for a nematically ordered homogeneous base-state [26]. As shown in Fig. 4a, the analysis reveals a wave-number of maximal growth, k_{cr} , along this direction, with k_{cr} growing with approximate linearity in $\alpha = \alpha_{aa} + \alpha_{pa}$. Also the plane-wave vector of maximal growth is aligned with the nematic director ($\theta = 0$ in Fig. 4a inset). By contrast, when solving a Stokes equation forced by a bulk stress, the velocity-stress relation in Fourier space becomes $\hat{\mathbf{u}} = \frac{i}{k}(\mathbf{I} - \hat{\mathbf{k}}\hat{\mathbf{k}})(\hat{\Sigma}^e \hat{\mathbf{k}})$. Comparing to our surface model, the factor of k in the denominator profoundly changes the nature of system stability, giving that maximal growth occurs at $k = 0$ for the bulk model, and so not producing a characteristic length-scale [22, 37]. (This was also noted by [38] in their study of swimmers confined to immersed thin films, while [39] show that adding substrate friction changes length-scale selection in 2D active nematic models.)

Figure 4b shows the nonlinear results of this linear instability. A series of cracks form along $\hat{\mathbf{y}}$, associated with moving fluid jets and bending of nematic field lines. In panel (b) inset, the spatial variations of the velocity field are in excellent agreement with the velocity eigenmode associated with k_{cr} for the linearized system. The distance between these cracks matches the half-wavelength, i.e., $\lambda_{cr} = \pi/k_{cr}$, which is in fact representative of the characteristic of the full dynamics of motile defects (Fig. 3a). At late times, panel (c) shows that these cracks lose stability, and eventually “break” to form defect pairs.

Discussion. We have explored other aspects of our model system. For example, when turning off hydrody-

namics in our kinetic model, we find polar lanes emerging as in our BD-MC model. This arises from a slow instability (consistent with the BD-MC model) when compared with hydrodynamic instabilities. We find that either active stress (aa or pa) taken individually will produce qualitatively similar flows and defect dynamics. Hence, the qualitative nature of the large-scale dynamics does not by itself isolate the precise origins of a destabilizing stress. An interesting aspect of our BD-MC study is that active stresses are extensile, which is very different from the contractility observed in actin-myosin gels [40]. This is likely related to the rigid MTs being in a nematically ordered state. While we applied our multiscale polar model to study experiments of synthesized active fluids, similar but more elaborated models might serve as a principled basis from which to study biological systems such as the eukaryotic mitotic spindle.

Acknowledgements. We thank D. Chen and D. Needleman for useful discussions. This work was funded by NSF grants DMR-0820341 (NYU MRSEC: TG, MS), DMS-0920930 (MS), EF-ATB-1137822 (MB), DMR-0847685 (MB), and DMR-0820579 (CU MRSEC: MG); DOE grant DE-FG02-88ER25053 (TG, MS); NIH grant R01 GM104976-03 (MB, MS); and the use of the Janus supercomputer supported by NSF grant CNS-0821794.

-
- [1] R. Voituriez, J. Joanny, and J. Prost, *Europhys. Lett.* **70**, 404, (2005).
 - [2] C. Wolgemuth, *Biophys. J.* **95**, 1564, (2008).
 - [3] S. Ramaswamy, *Ann. Rev. Cond. Matt. Phys.* **1**, 323, (2010).
 - [4] S. Fielding, D. Marenduzzo, and M. Cates, *Phys. Rev. E* **83**, 041910, (2011).
 - [5] H. Wensink, J. Dunkel, S. Heidenreich, K. Drescher, R. Goldstein, H. Löwen, and J. Yeomans, *Proc. Nat. Acad. Sci.* **109**, 14308, (2012).
 - [6] F. Nédélec, T. Surrey, A. Maggs, and S. Leibler, *Nature* **389**, 305, (1997).
 - [7] T. Surrey, F. Nédélec, S. Leibler, and E. Karsenti, *Science* **292**, 1167, (2001).
 - [8] V. Schaller, C. Weber, C. Semmrich, E. Frey, and A. Bausch, *Nature* **467**, 73, (2010).
 - [9] T. Sanchez, D. Chen, S. DeCamp, M. Heymann, and Z. Dogic, *Nature* **491**, 431, (2012).
 - [10] H. Nakazawa and K. Sekimoto, *J. Phys. Soc. Japan* **65**, 2404, (1996).
 - [11] K. Kruse and F. Jülicher, *Phys. Rev. Lett.* **85**, 1778, (2000).
 - [12] T. Liverpool, and M. Marchetti, *Europhys. Lett.* **69**, 846, (2005).
 - [13] F. Woodhouse and R. Goldstein, *Proc. Nat. Acad. Sci.* **110**, 14132, (2013).
 - [14] D. Head, W. Briels, and G. Gompper, *Phys. Rev. E* **89**, 032705, (2014).
 - [15] L. Giomi, M. Bowick, X. Ma, and M. Marchetti, *Phys. Rev. Lett.* **110**, 228101, (2013).
 - [16] L. Giomi, M. Bowick, P. Mishra, R. Sknepnek, and M. Marchetti, *arXiv:1403.5254*.
 - [17] S. Thampi, R. Golestanian, and J. Yeomans, *Phys. Rev. Lett.* **111**, 118101, (2013).
 - [18] S. Thampi, R. Golestanian, and J. Yeomans, *Europhys. Lett.* **105**, 18001, (2014).
 - [19] S. Thampi, R. Golestanian, and J. Yeomans, *arXiv:1402.0715*.
 - [20] R. Simha and S. Ramaswamy, *Phys. A* **306**, 262, (2002).
 - [21] M. Doi and S. F. Edwards, *The theory of polymer dynamics*, Oxford University Press, 1988.
 - [22] D. Saintillan and M. Shelley, *Phys. Rev. Lett.* **100**, 178103, (2008).
 - [23] G. Subramanian and D. Koch, *J. Fluid Mech.* **632**, 359, (2009).
 - [24] B. Ezhilan, M. Shelley, and D. Saintillan, *Phys. Fluids* **25**, 070607, (2013).
 - [25] K. Visscher, M. Schnitzer, and S. Block, *Nature* **400**, 184, (1999).
 - [26] See supplementary material [url], which includes Refs. [41-54].
 - [27] Y. Tao, W. den Otter, J. Padding, J. Dhont, and W. Briels, *J. Chem. Phys.* **122**, 244903, (2005).
 - [28] M. Allen and D. Tildesley, *Computer Simulation of Liquids*, Clarendon Press, Oxford, 1987.
 - [29] J. Keller and S. Rubinow, *J. Fluid Mech.* **75**, 705, (1976).
 - [30] G. Batchelor, *J. Fluid Mech.* **41**, 545, (1970).
 - [31] E. Tjhung, M. Cates, and D. Marenduzzo, *Soft Matter* **7**, 7453, (2011).
 - [32] M. Forest, Q. Wang, and R. Zhou, *Soft Matter* **9**, 5207, (2013).
 - [33] D. Axelrod, D. Koppel, J. Schlessinger, E. Elson, and W. Webb, *Biophys. J.* **16**, 1055, (1976).
 - [34] L. Giomi, L. Mahadevan, B. Chakraborty, and M. Hagan, *Phys. Rev. Lett.* **106**, 218101, (2011).
 - [35] L. Giomi and M. Marchetti, *Soft Matter* **8**, 129, (2012).
 - [36] S. Zhou, A. Sokolov, O. Lavrentovich, and I. Aranson, *Proc. Nat. Acad. Sci.* **111**, 1265, (2014).
 - [37] S. Ramaswamy (private communication).
 - [38] M. Leoni and T. Liverpool, *Phys. Rev. Lett.* **105**, 238102, (2010).
 - [39] S. Thampi, R. Golestanian, and J. Yeomans, *arXiv:1407.1211*.
 - [40] P. Bendix, G. Koenderink, D. Cuvelier, Z. Dogic, B. Koeleman, W. Briehar, C. Field, L. Mahadevan, and D. Weitz, *Biophys. J.* **94**, 3126, (2008).
 - [41] M. Bates and D. Frenkel, *J. Chem. Phys.* **112**, 10034, (2000).
 - [42] P. Bolhuis and D. Frenkel, *J. Chem. Phys.* **106**, 666, (1997).
 - [43] S. McGrother, D. Williamson, and G. Jackson, *J. Chem. Phys.* **104**, 6755, (1996).
 - [44] H. Löwen, *Phys. Rev. E* **50**, 1232, (1994).
 - [45] P. Bolhuis, A. Stroobants, D. Frenkel, and H. Lekkerkerker, *J. Chem. Phys.* **107**, 1551, (1997).
 - [46] F. Vesely, *J. Chem. Phys.* **125**, 214106, (2006).
 - [47] B. Alberts, A. Johnson, J. Lewis, M. Raff, K. Roberts, and P. Walter, *Molecular Biology of the Cell* 5th edition, Garland Science, New York, 2007.
 - [48] D. Wirtz, *Annu. Rev. Biophys.* **38**, 301, (2009).
 - [49] M. Schnitzer, K. Visscher, and S. Block, *Nat. Cell Biol.* **2**, 718, (2000).
 - [50] C. Coppin, J. Finer, J. Spudich, and R. Vale, *Biophys. J.* **68**, 242S, (1995).
 - [51] J. Brady, *J. Chem. Phys.* **98**, 3335, (1993).

- [52] G. Jeffery. Proc. Roy. Soc. Lond. Ser. A **102**, 161, (1922).
- [53] W. Maier, and A. Saupe. Zeit. Nat. Teil A **13**, 564, (1958).
- [54] C. Hohenegger and M. Shelley. Phys. Rev. E **81**, 046311, (2010).